RESEARCH ARTICLE | OCTOBER 19 2023

Modeling of the spray-induced wall stress acting on the ignition assistance device ⊕✓

Sayop Kim ⓘ ; Roberto Torelli ⓘ ; Surya Kaundinya Oruganti ; Je Ir Ryu ✉ ⓘ ; Tonghun Lee ; Kenneth S. Kim; Chol-Bum M. Kweon ⓘ

Check for updates

CrossMark

View Online

Export Citation

19 October 2023 11:31:27

Modeling of the spray-induced wall stress acting on the ignition assistance device EP

View Online · Export Citation · CrossMark

Sayop Kim,[1,2] (iD) Roberto Torelli,[2] (iD) Surya Kaundinya Oruganti,[2] Je Ir Ryu,[1,3,5,a] (iD) Tonghun Lee,[4] Kenneth S. Kim,[5] and Chol-Bum M. Kweon[5] (iD)

AFFILIATIONS

[1]Division of Engineering, New York University Abu Dhabi, Abu Dhabi, United Arab Emirates
[2]Transportation and Power Systems Division, Argonne National Laboratory, Lemont, Illinois 60439, USA
[3]Tandon School of Engineering, New York University, Brooklyn, New York 11201, USA
[4]Department of Mechanical Science and Engineering, University of Illinois at Urbana-Champaign, Urbana, Illinois 61801, USA
[5]Combat Capabilities Development Command Army Research Laboratory, Aberdeen Proving Ground, Maryland 21005, USA

[a]Author to whom correspondence should be addressed: jryu@nyu.edu

ABSTRACT

This research introduces a novel wall-stress model called the Spray-Induced Wall Stress (SIWS) model, which considers the effects of spray-wall impingement and the resulting formation of wall stress within the Lagrangian spray modeling framework. The primary objective of this paper is to provide a mathematical description of the fundamental physics underlying the model. Subsequently, the proposed model is validated using existing experimental data. The remainder of the study focuses on the practical application of the model to an ignition assistance device. Specifically, this device is installed in a compression ignition engine and designed to enhance ignition in aviation-fueled high-altitude aircraft propulsion systems. The research sheds light on the mechanical impulse caused by the high-speed impact of the spray jet, leading to the accumulation of mechanical stress on the rigid body of the ignition assistance device. Previous studies on fluid–structure interaction have only considered the interaction between the gas phase and the solid wall. However, the SIWS model incorporates the additional impact of the impinging liquid spray jet. Consequently, the simulated stress distribution on the ignition assistance device can be estimated by considering both the gas-phase-induced term and the spray-induced term simultaneously.

NOMENCLATURE

AMR	Adaptive mesh refinement
ARL	Army research laboratory
CHT	Conjugate heat transfer
CI	Compression ignition
CFD	Computational fluid dynamics
FEA	Finite element analysis
FSI	Fluid–structure interaction
RCM	Rapid compression machine
SIWS	Spray-Induced Wall Stress Model
C_{eff}	Dynamic conversion efficiency
dA_{cell}	Cell surface area facing the wall boundary
$d\vec{p}_{ij}$	Momentum change between a pair of impinging (i) and post-impinging (j) parcels
dt_{CFL}	Convective flow time scale, CFD time step
dt_{impact}	Characteristics impact time scale

$\vec{f}_{net}$	Net force applied by a single parcel impingement
$\vec{F}_{cell}$	Net force applied to the cell boundary surface area
$\vec{I}_{parcel}$	Impulse from a single parcel impingement
$\vec{\tau}_{cell}$	Spray-induced wall stress stored on the boundary cell
$\bar{\tau}_{ij}$	Turbulent mean viscous stress tensor
$\dot{\omega}_k$	Turbulent mean reaction rate of species, k

I. INTRODUCTION

Direct-injection compression ignition (CI) systems are commonly used in the ground transportation sector, and their advantages in ignition control and energy efficiency make them applicable to the development of Jet-A fueled piston aircraft engines.[1–3] This extends the benefits of traditional CI engine techniques to the aviation sector. However, designing aircraft engines for high-altitude conditions presents a challenge due to the varying oxygen levels at different

elevations.[4–6] Consequently, the ignition characteristics of jet fuels can change significantly with altitude.

The United States Department of Defense's Single Fuel Forward Policy[7] requires the dominant usage of jet fuels to reduce the significant logistic burden of managing and transporting multiple fuels. Consequently, aircraft CI engine development is limited to the limited choice of jet fuels. This poses a challenge as these fuels have low reactivity compared to the high-reactivity hydrocarbon fuels traditionally used in CI engines. For example, the commonly used aviation jet fuel F-24 has a low cetane number that ranges from 30 to 52.[1,8] The combination of low reactivity and high-altitude operation can lead to unstable engine combustion, misfire, knocking, and power loss.[9] To address these issues, an ignition assistance device that actively controls ignition is preferred.

There are two main types of active ignition control strategies: mixing control and thermal-energy deposit methods. The mixing control method focuses on enhancing fuel–air mixing through strategies like pilot injection[10] and multi-mode combustion control.[11] The thermal-energy deposit method involves preheating the mixture, typically using an ignition assistance device such as a glow plug. In this method, the electronically powered ignition assistance can create a preheating ignition source (i.e., thermal boundary layer) in the combustion chamber before the fuel injection and is popularly used in land-based engine systems for cold-start operations.[12–14] This can also benefit jet-fueled aircraft engines in high-altitude operations. Recent experimental and numerical studies[15–22] have explored the application of ignition assistance systems in this context, investigating fuel variability and optimizing ignition assistance device parameters. Motily and co-workers[22,58] examined the fuel variability using a light-duty CI engine at increased elevations. Using the high-heating ignition assistance device, the sensitivity of the cetane number was observed to be reduced. Ryu and his co-workers[18–20] have performed experiments and numerical simulations and characterized the representative ignition modes as a function of the electric power input in the ignition assistance device. They further exercised a similar test campaign to optimize the critical ignition assistance device operating parameters by employing a design of experiment (DoE) method.[21,59]

Unlike cold-start operations in land-based CI engines, the ignition assistance device in aircraft engines needs to be constantly activated while the engine is running. Consequently, the device undergoes intense thermo-mechanical cycling with significant temperature and pressure variations on its surface. This can lead to mechanical breakdown, corrosion, oxidation, and short circuits. Prior studies[23–25] have focused on durability analyses of ignition assistance devices, identifying factors contributing to system failure and proposing solutions to improve durability. The research led by Oprea et al.[23] showed durability test results on a hot surface of the ignition assistance device for natural gas direct-injection CI engines. One of their important findings is that the primary factor contributing to the system failure is the mix of thermo-mechanical and chemical processes around the hot surface and the electric circuit's internal component. Motily[24] conducted several durability tests to assess the failure modes of the ignition assistance device equipped with a rapid compression machine (RCM). Mechanical breakdown of the ignition assistance device was due to overheating, internal conductor breakdown, surface oxidation associated with the applied electric circuit voltage, and operational abuse. It was also found that extreme combustion events inside the combustion

chamber can degrade the durability of the ignition assistance device. Karpe et al.'s study[25] focused on describing the failure phenomena of the ignition assistance device during the diesel cold-start and follow-up attempts to extend the system lifespan. They discovered the most vulnerable component of the ignition assistance device within its heating coil element and concluded that aluminizing the heating coil can improve the system's durability.

The critical components of the ignition assistance device are exposed to high temperatures and pressures. The device's hot-temperature surface is repeatedly impacted by high-speed spray flames. This extreme thermo-mechanical cycling can accelerate system body fatigue through impact loading. Such multi-physics phenomena can be numerically exercised with the aid of fluid–structure interaction (FSI) analysis, which combines computational fluid dynamics (CFD) and finite element analysis (FEA), namely, coupled CFD-FEA method. The CFD solver is responsible for describing the thermal-fluid elements flowing around the ignition assistance device. Then, the FEA solver can import the transient thermo-mechanical boundary conditions from the CFD simulations and sequentially solve the governing equations for thermoelastic solid materials of interest. The FSI analysis has been widely applied in various engineering applications, such as gas turbine component design,[26–29] cylinder head design,[30,31] brake rotor cooling, and subsequent stress analysis.[32–34] These reference studies characterized the thermo-mechanical stress of the high-temperature and high-contact-pressure applications.

Recent studies[35,36,60] exploited the CFD-FEA coupling workflow to investigate the impact of high-pressure spray flames on the stress behavior of ignition assistance device surfaces. The novelty of their workflow can be acknowledged by the capability of capturing the spatiotemporal boundary conditions on the interface, which is a lacking feature in the traditional semi-empirical method. A phenomenological heat-flux model was also employed in their analysis to account for the self-sustained heating in the ignition assistance device, which could be an additional source of thermal stress. In the proposed workflow, they first performed three-dimensional CFD simulations, wherein the ignition assistance device is equipped with the combustion chamber. Then the transient profile of thermo-mechanical properties on the ignition assistance device interface was mapped onto a finite element data structure; thus, it enabled coupled FEA simulations. Their simulation results capture thermal shock events caused by spray impingement and subsequent flame sweep around the system body. The spray impingement and subsequent cooling over a short time span can result in a rapid thermal stress drop. Such a spray-induced thermal shock was restricted to the concentrated area of the spray-impinging region. In contrast, the ignition and flame-induced thermal shock caused a significant thermal stress increase over a wide surface area. Hence, they concluded that the thermal shock event is the dominant process.

Despite the observable spray impact on the wall-stress establishment, to the authors' best knowledge, none of the studies published to this date has addressed the spray-wall contact dynamics as a direct source of wall stress. Most prior studies dealing with the spray-wall impingement merely focused on the droplet internal flow change during the spray-wall contact, and the subsequent outcome such as droplet splash and film formation.[37–39] Likewise, none of the CFD software to this date incorporates the mechanical stress formation in the spray-wall interaction models. For that reason, today's CFD framework lacks the direct spray impact in the wall-stress calculation but merely

incorporates the aerodynamics force,[40] which is accompanied by the spray plume development. Therefore, today's CFD framework does not consider the impinging droplet's mechanical force acting on the wall. To bridge this gap, this study aims to develop a new capability within the Lagrangian spray modeling framework that can accommodate the source of the wall-stress as a direct outcome of the spray-wall contact. To achieve this, a Spray-Induced Wall Stress (SIWS) model is proposed, which accounts for the mechanical impact caused by the spray on the buildup of wall stress. This new sub-physics model has been implemented into the CFD solver, CONVERGE.[47]

It is rare to find benchmarking studies that can quantify the mechanical force of the single droplet impacting on the solid wall. Alternatively, prior experimental studies[41–46] can provide the integrated momentum flux contributed from an impinging spray jet. They conducted the pressure transducer measurement to evaluate the rate of momentum of diesel sprays at the atmospheric conditions. While these measurements were originally intended to identify the injection-rate profile of the tested injectors, they can also be viewed as a time integral of the net force exerted on the wall, representing a source of normal stress on the impacted wall. It is important to mention that the proposed SIWS model is to mimic the mechanical impacts resulting from the liquid droplet impingement event. It does not take into account the thermal diffusion aspect that may become significant in the form of spray cooling or thermal shock under extreme ambient conditions. To solely consider the mechanical aspect, therefore, the atmospheric conditions cast by the chosen experiment[41] are relevant for the purpose of the model validation. The test was performed using a configuration involving a single-hole injector and spray-jet impingement. Leveraging the functionality of the SIWS model, the remaining sections of the paper discuss the distribution of spray-induced wall stress on the surface of the ignition assistance device. The quantitative analysis aims to demonstrate the comparative significance of the spray-jet impact compared to the gas pressure impact in the analysis of wall stress.

II. SPRAY-INDUCED WALL STRESS MODEL: ARL-SIWS MODEL

The proposed ARL Spray-Induced Wall Stress (ARL-SIWS or SIWS hereafter) model is designed to account for the formation of wall stress caused by spray-wall impingement process. This model adopts the Lagrangian discrete phase approach to simulate a group of liquid particles impacting the wall. In this methodology, the particles are represented as computational parcels. The SIWS model has been incorporated into the CONVERGE CFD code as a subroutine utilizing a user-defined function (UDF). This SIWS model keeps track of the changing properties of the parcels as they hit the wall, i.e., impinging parcels. Subsequently, the properties of these parcels after impact, i.e., post-impinging parcels, are then included in the evaluation of wall stress.

The UDF has been integrated into the drop-wall interaction routine within the CONVERGE code, which encompasses various post-impingement scenarios, such as rebound, sliding, and splashing. Subsequently, the routine identifies the type and behavior of the parcels after impingement. These post-impinging parcel types include film parcels and splashed parcels, as shown in Fig. 1. Splashed parcels move away from the wall and are characterized by their size and velocity after impingement. To this end, the O'Rourke[48] model from the CONVERGE is employed to determine the characteristics of the post-impinging parcels. Detailed information regarding the O'Rourke
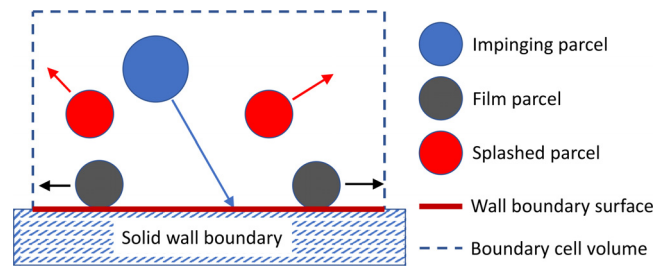

FIG. 1. Schematic of impinging parcels and post-impinging parcels in the boundary cell faced to the solid wall.

model's description can be found in the CONVERGE manual,[47] as it falls outside the scope of this paper.

The SIWS model's underlying assumption is based on the momentum transfer between discrete spray parcels and wall boundary during the impingement incident. The transferred momentum can be determined by the net change of the momentum retained by the impinging parcel and the subsequent post-impinging parcel. In this development routine, net mechanical force ($\vec{f}_{net}$) applied by a single parcel impingement is assumed to act on the embracing cell's wall boundary surface area (dA_{cell}). The wall-impingement event may occur in a characteristics impact timescale (dt_{impact}). Thus, the transmitted impulse to the cell boundary can be formulated as follows:

$$\vec{I}_{parcel} = \vec{f}_{net}\, dt_{impact}. \tag{1}$$

Indeed, the parcel-wall impingement is a mechanical contact between the two separate phases and is very instantaneous. Thus, the impact timescale must be a sub-physics timescale and, generally, smaller than the convective timescale (dt_{CFL} and CFD time step, dt, hereafter). Although a precise impact timescale can be formulated based on particle kinetics theory, the present work substitutes the dt_{impact} term with the dt to avoid a computationally intensive time-integration routine.

Note that the impinging parcel is paired with the post-impinging parcel in the corresponding boundary cell, and the impulse determined by Eq. (1) equates to momentum change ($d\vec{P}_{ij}$) between the pair, i and j, i.e., parcel identifiers for impinging and post-impinging parcels, respectively. As such, the net impulse acting on the boundary cell surface over the time step, dt, can be algebraically calculated by an integral of the momentum change for every pair of the impinging and post-impinging parcels that can be effective during the CFD time step and expressed in Eq. (2). As the total force acting on the cell boundary surface is denoted by $\vec{F}_{cell}$ and impact timescale is dt, Eqs. (2) and (3) derive the wall-stress component effective on the cell boundary surface area.

In this context, the model utilizes an empirical constant denoted as C_{eff} to account for the dynamic conversion efficiency. This factor takes into consideration the efficiency of converting mechanical energy and introduces an aspect related to the loss of mechanical energy during the impingement event. For example, when a liquid parcel impacts, some of the mechanical energy it possesses may be dissipated due to factors such as spray cooling and other mechanisms that lead to energy loss, especially under extreme ambient conditions. In the present test, this constant was set to be unity, implying that there is no mechanical energy loss while transferring the momentum. This assumption holds well under the specific conditions of atmospheric pressure and low

temperature condition, which is considered for the model validation test. However, it is worth noting that in a practical combustion chamber environment, this constant can be adjusted by the user to accommodate and address the impact of energy dissipation more flexibly.

$$\vec{I}_{cell} = \sum_{ij} \vec{I}_{parcel, ij} = \sum_{ij} dp_{ij}, \quad (2)$$

$$\vec{I}_{cell} = \vec{F}_{cell}\, dt, \quad (3)$$

$$\vec{\tau}_{cell} = \frac{C_{eff}\, \vec{I}_{cell}}{dt\, dA_{cell}}. \quad (4)$$

III. TEST CONDITIONS AND SIMULATION SETUP

In this section, two distinct test campaigns are employed. The first test focuses on validating the model using single-hole diesel injectors. The goal is to determine the optimal setup for the CONVERGE model that yields accurate results across various spray conditions. The test covers spray configurations that involve freely evolving sprays without impingement as well as sprays that impinge on walls. Building upon the insights gained from the first test, the second test incorporates the combustion chamber domain with the ignition assistance device. This test includes both non-reacting and reacting sprays to analyze wall stress.

A. Best practice of CFD model setup

For all the test conditions, three-dimensional Reynolds-Average Navier–Stokes (3D RANS) simulations were conducted using the CONVERGE CFD solver. The simulations employed a pressure-implicit with splitting of operators (PISO) algorithm and a flux-blending finite volume method. The computational domains were constructed using a consistent meshing strategy with a base grid scale of 8 mm and a minimum grid scale of 0.125 mm. Achieving the minimum grid scale involved applying a 5-level grid refinement that combined adaptive mesh refinement (AMR) with fixed embedding mesh. This multi-layer grid refinement ensured suitable grid resolution for capturing the details of the high-speed spray jet plume. The optimal level of grid refinement was determined through a preliminary mesh-sensitivity test that compared the spray penetration length to measured data, as will be discussed in Sec. IV.

In the Lagrangian spray modeling aspect, computational parcels representing the spray were injected through the nozzle hole into the domain. To accurately represent the dense spray plume, a total of 512 000 parcels were generated sequentially during the injection duration. The subsequent processes of atomization, evaporation, and wall interaction were accounted for using the Kelvin–Helmholtz–Rayleigh–Taylor (KH-RT) model,[49] Frossling model,[50] and O'Rourke model,[48] respectively. The empirical constants required for these spray models were adopted from the default setup of CONVERGE, which is typically well-suited for high-pressure diesel injectors. In terms of modeling the continuum phase mixing, the turbulence closure was achieved using a gradient transport assumption and introducing turbulence viscosity based on a standard k-ϵ model.

B. Model validation test

This test aims to ensure the accuracy of the model in capturing the relevant quantity of wall stress, which depends on the momentum

flux applied to the specific wall component of interest. To validate the simulation results, they are compared with experiments conducted on high-pressure diesel injectors that measured the momentum flux using a pressure transducer downstream of the injector nozzle. Payri et al.[41] developed a measuring apparatus specifically for determining the impingement force of a spray jet. For the present study, the available test conditions from Payri's work, which include measurements of spray length and momentum flux, are employed and summarized in Table I.

While Payri's paper[41] provided the nominal injection duration (i.e., injector signal duration), the actual injection duration through the nozzle hole was not provided. However, their measured momentum flux profile can be used to determine the actual injection duration and rate profile for the Lagrangian injector boundary condition. It is important to note that Payri's experiment used the term "momentum flux," but in recently published papers,[43,44] the term "rate of momentum" has been interchangeably used and better reflects the physical property being targeted. Therefore, the term rate of momentum will be used throughout this paper.

C. Ignition assistance device setup in a rapid compression machine (RCM) test

In pursuit of the ignition assistance device wall-stress analysis, 3D RANS simulations were performed applying the SIWS model. The purpose of this test is to raise awareness regarding the mechanical rigidity of the ignition assistance structure. The analysis can be conducted by tracking the concentrated wall stress resulting from the direct impact of the spray plume and the explosive combustion event. It is important to highlight that the wall stress within the area of concern cannot be measured, and as a result, there is currently no existing compatible experimental data. Consequently, a comprehensive validation of the model in this testing setup is not feasible. Nevertheless, this test serves to underscore the importance of addressing the real-world mechanical resilience of the device.

The present RCM test rig with the ignition assistance system has been thoroughly investigated in the prior experiments[18–22] for the military purposed small aircraft engine development. Thus, the benchmarking test employed in this study can represent the practical aviation engine-like conditions. The ignition assistance device is positioned longitudinally in the RCM combustor domain, with its end-tip located 1 mm away from the injector axis. This positioning allowed the vertically evolving spray plume to impact the end-tip. The ignition system was installed at two different downstream locations, namely, 11 and 21 mm.

The 21 mm downstream location was originally designed to precisely benchmark the prior experiment. This setup was intended to

TABLE I. Test conditions used for the model validation.

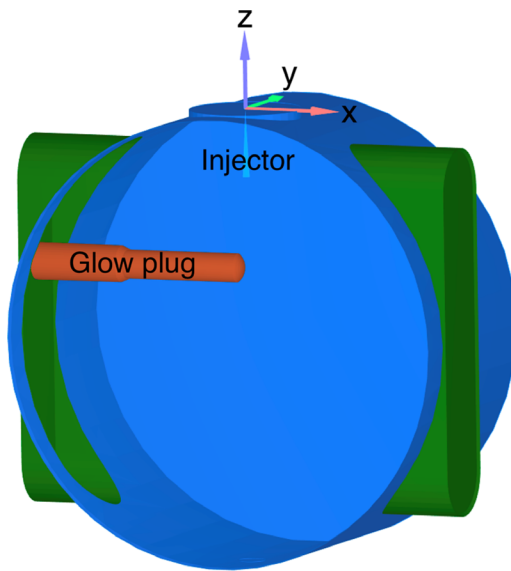| Injector ID	A	B	C
Nozzle hole diameter (μm)	112	137	156
Injection pressure (MPa)		30 and 80	
Ambient pressure (MPa)		3.5	
Ambient air temperature (°C)		25	
Injection duration (ms)		2.0	

FIG. 2. Geometrical configuration of the combustion chamber with the BERU glow plug component and single-hole injector setup.

avoid intense liquid plume impingement on the system device as the Ryu *et al.*[18] reported the liquid penetration measurement of 21.5 mm from their experiment and simulation tests. The 11 mm downstream location is added to realize the more intense liquid-wall impingement scenario in the present test. Non-reacting spray and reacting spray are considered for all tests. For the non-reacting spray test, an inert gas (N_2) was used without activating the electric circuit. For the reacting spray test, air was filled in the combustion chamber and the ignition system was activated with the selected electric voltage. The complete geometric configuration is depicted in Fig. 2, and the dimensions of the domain and test conditions are specified in Table II.

To conduct the reacting-spray test, two separate CFD simulations were performed to represent sequential events: (1) activation of the ignition assistance device and formation of the thermal layer, and (2) fuel spray and subsequent combustion. Separating these processes is beneficial because the timescale for diffusion/convection heat transfer significantly differs from that of high-pressure spray-induced

turbulence and associated chemistry. As a result, a large time step simulation could be allowed for the first simulation without sacrificing accuracy. In order to replicate the first event, the electric-circuit-activated ignition assistance device was modeled to resemble an actual BERU glow plug utilized in the benchmarking experiment.[51]

The preheating process in the ignition assistance device was governed by the heat flux model.[35,36] The conjugate heat transfer (CHT) model was utilized to account for subsequent heat transfer through the solid materials. The combustion chamber domain was initially filled with air at a temperature of 800 K and a pressure of 3 MPa. The simulation was conducted without fuel injection for a duration of 30 s of physical time to ensure a steady state, representing the formation of the thermal boundary layer around the ignition assistance device. Once the ignition assistance device reached a steady-state surface temperature, F-24 jet fuel was injected toward the tip location of the device, simulating the second event involving fuel spray and subsequent combustion. The ignition and combustion events were modeled using a well-stirred reactor (WSR) combustion model available in CONVERGE, and the detailed chemistry of the F-24 jet fuel was handled by a recently developed data-driven F-24 Fuel chemistry[52] based on the HyChem approach.[53]

IV. RESULTS AND DISCUSSION
A. Validation of the employed model

In order to achieve reasonable predictive accuracy within the Eulerian–Lagrangian framework, it is necessary to test the setup of the Lagrangian spray model on an appropriate mesh size that can capture the transient evolution of the spray plume. The following test focuses on investigating the sensitivity of the predicted spray penetration length to the grid size. Provided with a base grid scale of 8 mm, multiple levels of grid refinement techniques were applied to accurately represent the observed spray penetration length pattern from experiments. As illustrated in Fig. 3(a), when using a coarse grid scale (e.g., 1.0 mm), the spray penetration length is under-resolved, leading to an inadequate representation of momentum exchange between the liquid spray and the surrounding gas. However, as the grid scale is refined, the model setup is able to recover the experimentally observed pattern of spray penetration.

Figure 3(b) displays the difference between the predicted data and the measured data shown in Fig. 3(a), using the Hausdorf distance[54] as a metric. This metric is used to evaluate the dissimilarity

TABLE II. Dimensions of the combustion chamber, ignition assistance device component, and electric circuit voltage input for the heating element.

Combustion chamber domain	Radius I	25.4 mm
	Depth (D)	26 mm
	Filled gas temperature (T)	800 K
	Filled gas pressure (P)	3 MPa
	Gas composition (non-reacting/reacting) (vol)	N_2 (100%)/O_2 (23%), N_2 (77%)
BERU glow plug	Type	Co-annular type heat core
	Heat core material (composition)	Ceramic (SI_3N_4 54%, $MoSI_2$ 46%)
	Tip radius I	2.74 mm
	Tip horizontal location	1 mm from the injector axis
	Tip vertical location	11 mm, 21 mm from injector hole
	Electric circuit voltage input (V)	7 (reacting case)

(a) Spray penetration length
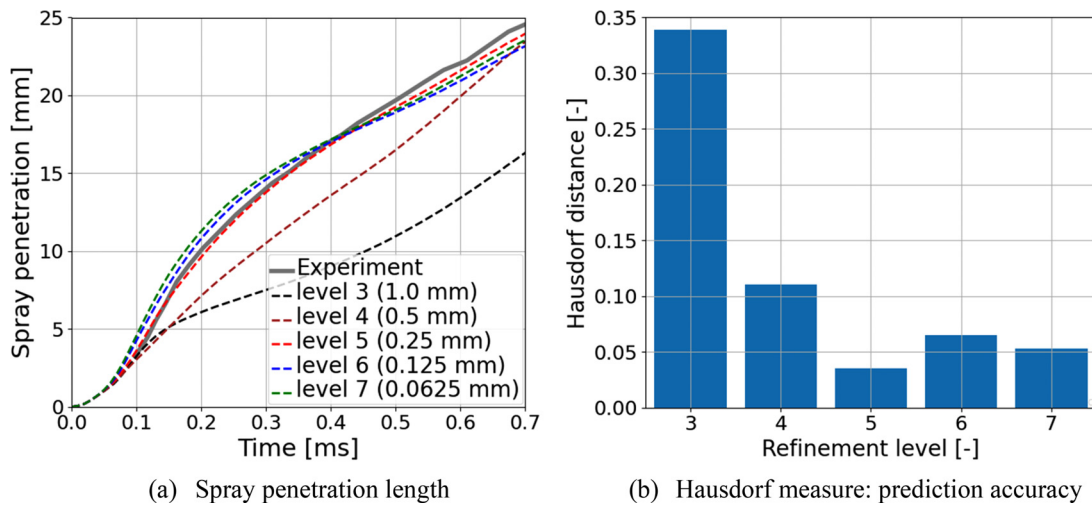
(b) Hausdorf measure: prediction accuracy

FIG. 3. Preliminary grid size sensitivity test: (a) spray tip penetration length comparison between the current CFD setup and the experiment[41] and (b) corresponding prediction accuracy.

between two datasets and quantifies the distance between two subsets in a metric space. A higher Hausdorf distance indicates a poorer prediction. In this test, two subsets were created, one from the experimentally observed spray penetration curves in Fig. 3(a) and the other from the numerically resolved spray penetration curves. Each subset consists of a two-dimensional array representing spray length vs time. To remove dimensional bias, both length and time were renormalized, resulting in a dimensionless value for the Hausdorf distance. The results show that the refinement level of 5 provides the best accuracy with the smallest Hausdorf distance among all the tested grid refinement levels. The poorer results observed with finer meshes (e.g., 6 and 7 levels) are attributed to the under-resolved drag force when the grid size becomes comparable to or smaller than the nozzle diameter (approximately 0.1 mm). This tendency is particularly evident during the first 0.35 ms of the simulation, as depicted in Fig. 3(a). Based on this analysis, the subsequent test cases utilize a grid refinement level of 5 as the optimal grid resolution.

As listed in Table I, the validation test conditions consist of two different injection pressures (30 and 80 MPa) and three different injectors used for model validation. Employing the best-practiced grid refinement setup, the following tests encompass two distinct validation experiments. The first test aims to verify the basic Lagrangian spray model used. The predictive accuracy is assessed by comparing the spray penetration length with available experimental data.[41] The results presented in Fig. 4 demonstrate that the employed Lagrangian model setup, in conjunction with the optimal grid refinement, effectively captures the relevant spray momentum.

The second test aimed to compare the rate of momentum estimated by the SIWS model with the corresponding measurement.[41] The test involved an impinging spray configuration with a 5 mm distance of impact. In the experimental setup, a pressure transducer was used to provide a stagnation wall that was impacted by the impinging spray and measured the spray impulse. The measured data represent the rate of momentum and are expressed in units of force (N). Figure 5 presents a comparison between the CFD simulations and the corresponding measurements. The simulated results

obtained using the SIWS model show good agreement with the experimental measurements.

In the simulations, the rate of momentum is determined as a result of the combined impact of gas-phase pressure and spray-induced impulse. It is worth noting that a high-speed turbulence gas-jet can coexist with the high-pressure spray jet. It is commonly observed that there is a significant gas entrainment into the upstream region of the spray core, where the high-flux liquid jet is present. This gas entrainment forms a turbulence gas-jet that evolves alongside the spray jet. Consequently, both the spray jet and the gas jet mechanically impact the wall simultaneously. To account for this phenomenon, the
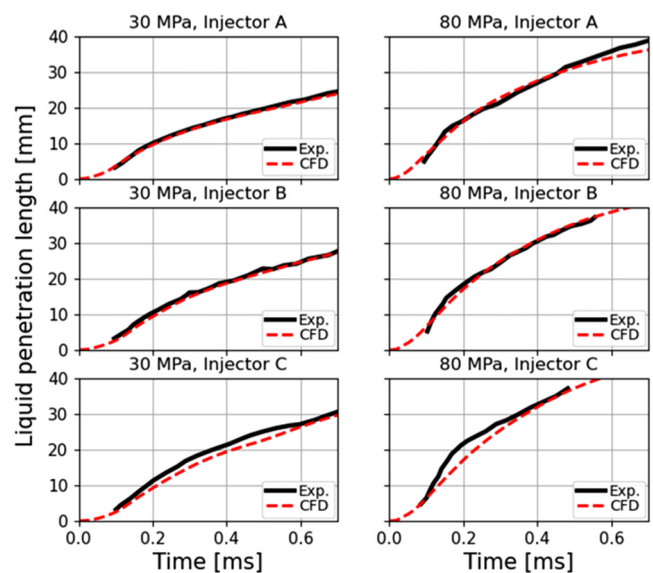

FIG. 4. Spray tip penetration length comparison between the current CFD setup and the experiment.[41]
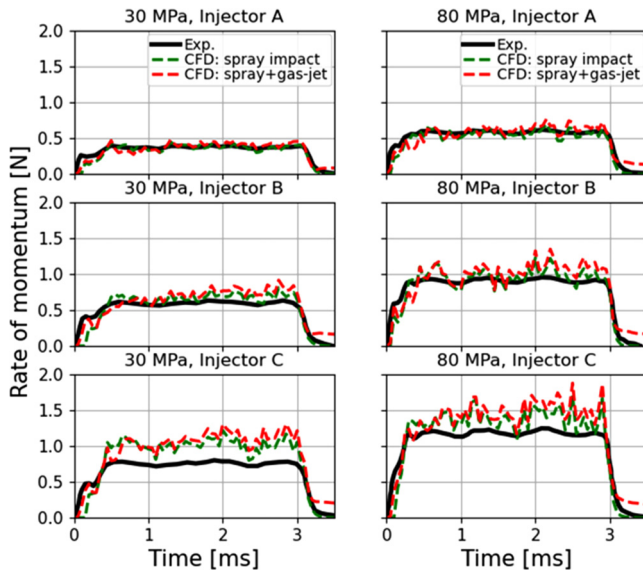
FIG. 5. Comparison of the rate of momentum between the current CFD setup and the experiment.[41]

overall rate of momentum. On the other hand, there is a residual gas-jet inertia present in the simulations after 3 ms, which is not observed in the experiment. However, the SIWS model is able to reasonably predict the level of the rate of momentum.

In Fig. 6(a), the wall stress induced by the spray-jet is depicted using contour colors, which represents the output of the SIWS model prediction. Additionally, Fig. 6(b) illustrates another component of wall stress caused by the gas-jet impingement, specifically in the form of gas static pressure applied to the wall. It is interesting to note that both the spray-jet and gas-jet reach maximum stress levels of approximately 5–6 times the pressure unit, with the stress levels being an order of magnitude higher than other measurements. To provide a more detailed quantification, Fig. 7 displays the time-averaged distribution of wall stress separately for the gas-jet and spray-jet impacts. Each individual measurement point is defined at intervals of 0.3 mm in the cross-spray direction, collecting the wall stress values from neighboring boundary cells. The light gray dots represent the instantaneous wall-stress profile at intervals of 0.1 ms. In this particular test, the liquid particles have not undergone complete atomization or evaporation due to the short impact distance (5 mm from the injector nozzle). As a result, the wall stress induced by the spray-jet outweighs the impact from the gas-jet by a factor of 2.

Meanwhile, in Fig. 7, it is evident that the gas-jet's influence (i.e., gas phase dynamic pressure) on wall stress cannot be considered insignificant, despite the earlier observation in Fig. 5 suggesting a marginal level of gas-jet-induced rate of momentum. This disparity arises from the fundamental difference in the definitions of wall stress and momentum rate. Wall stress is a localized measure, whereas momentum rate is calculated by integrating pressure (i.e., normal stress) across the entire wall surface. Consequently, negative pressure regions can be observed beyond the effective jet-impinging region with a radius of
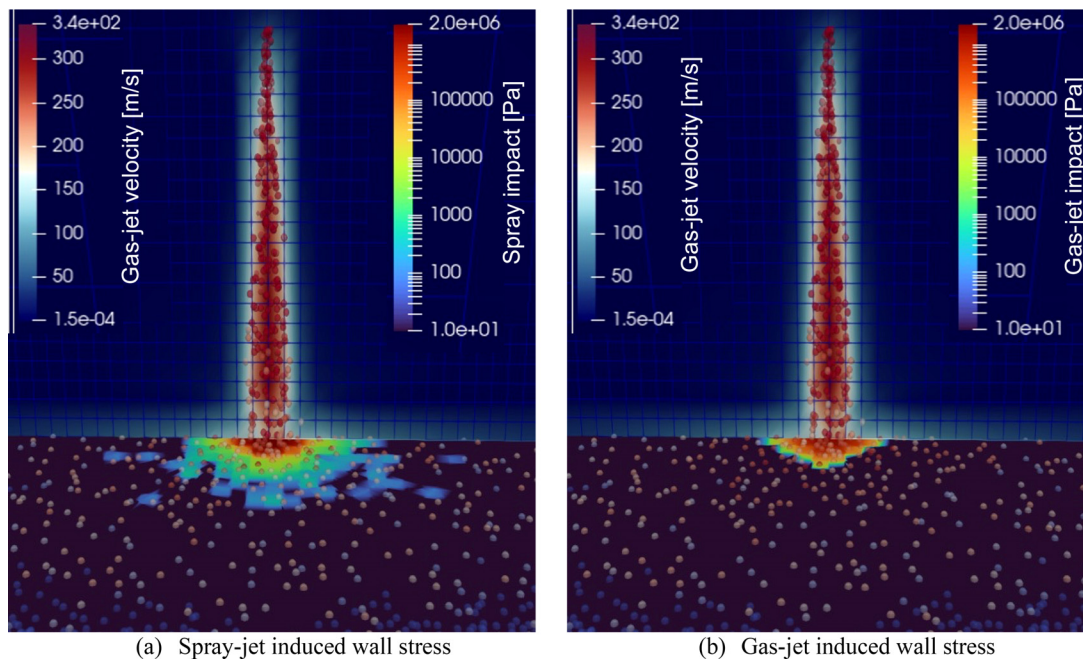
rate of momentum values shown in Fig. 5 are represented as the sum of the impacts from both the gas-phase pressure and the spray (red curves), as well as the sole impact of the spray (green curves). Since the wall must maintain mechanical equilibrium due to the initial gas pressure, the gas-phase pressure impact is expressed as the relative pressure term relative to the initial chamber pressure of 3.5 MPa. It is worth noting that the gas-jet impact contributes only a marginal value to the

(a) Spray-jet induced wall stress

(b) Gas-jet induced wall stress

FIG. 6. (a) Spray-jet-induced and (b) gas-jet-induced wall stress. The test was performed at an injection pressure of 80 MPa using injector A.
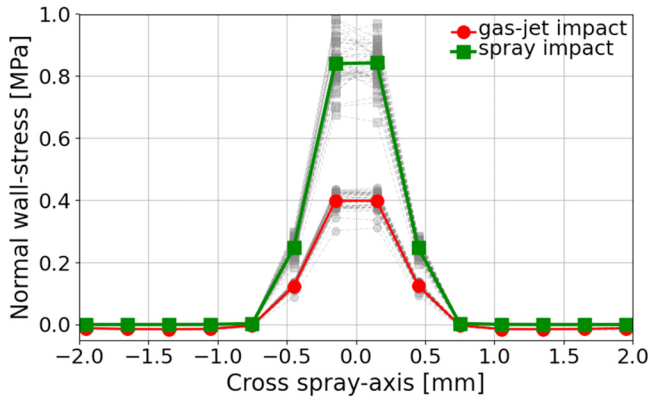
FIG. 7. Time-averaged wall-stress distribution in a cross spray-axis direction. The time average was taken over the injection duration.

0.75 mm in Fig. 7. This occurrence is a result of the counter-flow impact. Therefore, these negative pressure regions compensate for the substantial normal stress at the stagnation point (i.e., the impinging region), resulting in only a minor impact on the momentum rate.

The subsequent analysis examines potential reasons for the discrepancy observed in the rate of momentum curves in Fig. 5. It is observed that the SIWS model tends to overestimate the quantity as the size of the injector hole increases, as seen with injector C. This

trend remains consistent even when different droplet splash models available in CONVERGE, such as the Bai–Gosman model[55] and Kuhnke model,[56] were tested in the authors' preliminary investigations (which are not included here to avoid redundant discussions). Therefore, this behavior is likely attributed to the simplified assumption made in the SIWS model. The model lacks the incorporation of complex physics involved in the deformation and breakup of large-volume droplets.

In the SIWS model, the mechanical impulse gained by the wall boundary is perfectly converted from the momentum of the impinging particles, as expressed in Eq. (3). However, in reality, liquid droplet impingement may involve irreversible dissipation of mechanical energy, leading to an increase in droplet surface energy due to splashing and subsequent breakup processes. The extent of this energy dissipation should be influenced by the volumetric scale of the impinging particles. Additionally, it is possible that a portion of the internal viscous flow energy is converted into thermodynamic internal energy, and this effect is expected to be more pronounced when the mass of the impinging particle is higher. However, the SIWS model does not account for such complex physics at present. In this context, the following discussion explores the impact of droplet size in the vicinity of the wall boundary.

Figure 8 illustrates the joint probability density function (PDF) concerning particle velocity and size. The analysis focuses on the velocity component perpendicular to the wall, with liquid parcels collected from the boundary cells prior to wall contact and excluding post-
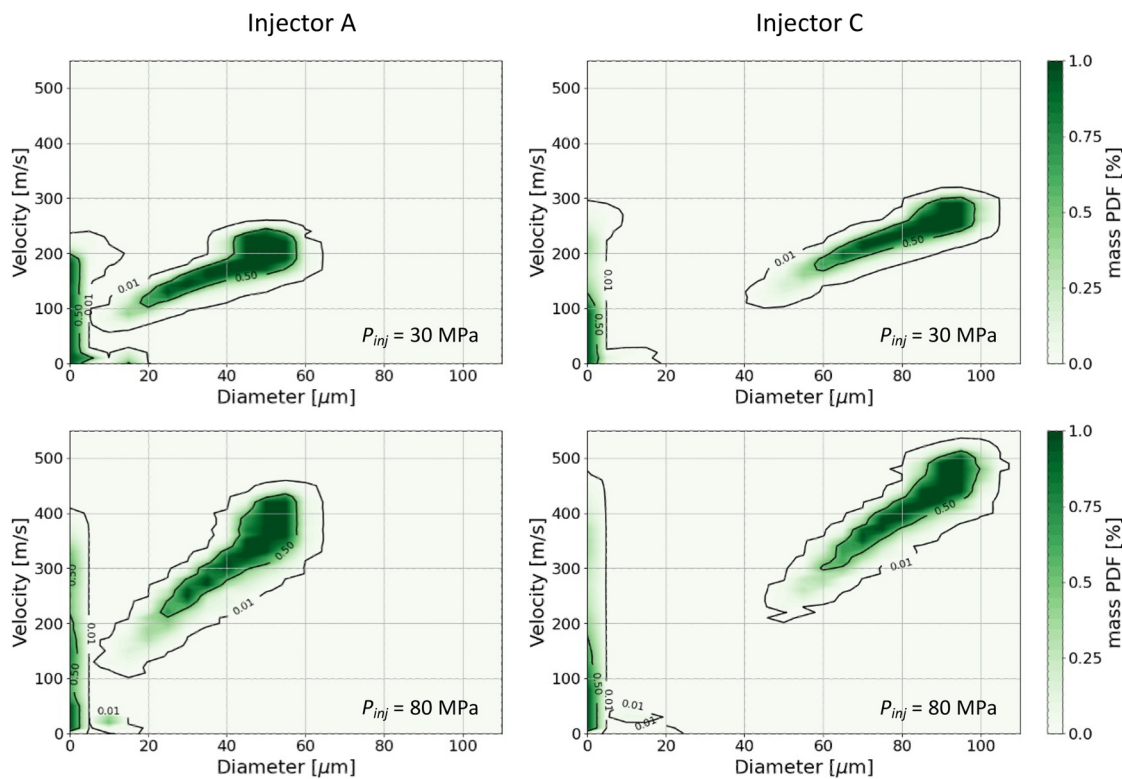

FIG. 8. Joint PDFs of spray particle diameter and velocity using injector A (left) and injector C (right) under two different injection pressure.

impinging (splashed) parcels. Two different injectors, referred to as injector A and injector C, are compared to represent particle clouds with small and large volumes, respectively. Additionally, two injection pressures of 30 and 80 MPa are considered. Given the relatively shallow impact distance of 5 mm in this test, the region of interest is primarily within the intact core region of the spray jet. This is evident from the distinct bimodal size distribution observed on the diameter axis. Each group within the distribution represents child parcels generated by the KH-RT breakup model,[49] as well as parent parcels that have undergone the spray jet-breakup process within the intact core region. The shape of the bimodal distribution is solely determined by the injector type, specifically the size of the injector hole, while the injection pressure only influences the range of the velocity distribution.

In contrast, the size of the child parcel group is significantly smaller. This suggests that the flow of the child parcel cloud can be characterized by a low Stokes number flow, allowing it to be suspended by the ambient gas flow without making direct contact with the wall. Consequently, the impulse gained by the wall is primarily attributed to the impact from the parent parcel cloud. As depicted in Fig. 8, injector C contributes a substantial volume of parcels to the wall impingement, indicating a more complex mechanical energy dissipation process. This complexity, inherent in the actual physics, has not yet been incorporated into the SIWS model and is, therefore, a primary factor contributing to the overestimation of the rate of momentum in cases involving injectors with larger diameters.

The utilization of the Lagrangian-based wall-stress model may introduce a potential numerical artifact that can have a significant impact. This artifact becomes evident in the noisy curves observed in Fig. 5 and the patchy distribution of stress contours displayed in Fig. 6(a). The cause of these artifacts is the relatively low cloud density of the injected parcels within the computational domain, which is considerably lower than that of realistic spray clouds encountered in practical applications with high-pressure injectors.

To address this issue, a parcel number resolution test is conducted, as illustrated in Fig. 9. Different orders of magnitude are employed to vary the total number of injected parcels, including 51 200, 512 000, and 5 120 000, representing coarse, baseline, and dense cloud representations, respectively. It is observed that a low number
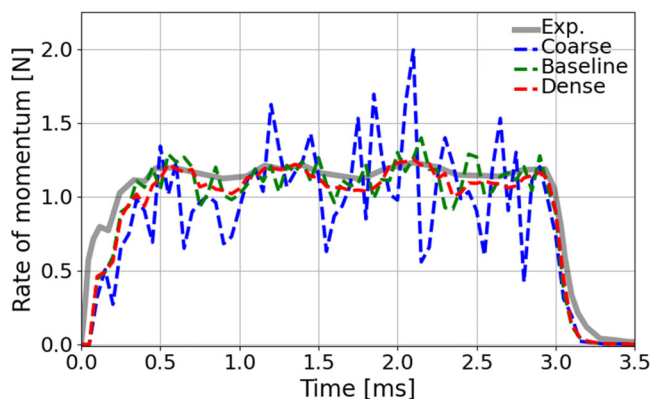

FIG. 9. Sensitivity of parcel number density on the calculated wall stress ($P_{inj} = 80$ MPa, Injector C). Injected parcels are 51 200, 512 000, and 5 120 000 for coarse, baseline, and dense parcel cloud tests.

density leads to a poor representation of the rate of momentum profile, while the highest number density helps to reduce the noise in the curve. However, for the sake of computational efficiency, the best practice test utilizes the baseline parcel number, which strikes a reasonable balance between accuracy and computational load.

B. Wall-stress test on ignition assistance device: Non-reacting case

The following discussion highlights an important aspect of using the SIWS model for analyzing the structural behavior of ignition assistance devices. A non-reacting spray scenario is considered, with an inert gas environment (specifically nitrogen) and no activation of the heating element. By employing the SIWS model, it becomes possible to conduct a meaningful structural analysis of the ignition assistance device component and quantify the stress levels resulting from the direct contact of the spray jet with the wall. Additionally, the gas phase static pressure adjacent to the wall contributes an additional source of wall stress. Similar to the previous test, a relative pressure field is utilized to assess the wall stress induced by the gas jet, with calculations performed relative to the initial gas pressure of 3 MPa. In this particular test, the tip of the ignition assistance device's heating element is positioned at two different impact distances, namely, 11 and 21 mm downstream of the injector nozzle, denoted as D_{impact}. As a result, the varying levels of spray-jet-induced wall stress can be observed depending on the impact distance.

Figure 10 displays the normal component of the spray-jet-induced and gas-jet-induced stresses on the wall component of the ignition assistance device after 2 ms from the start of injection, representing a steady-state phase. In parallel, a contour depicting the velocity of the gas jet is provided in a vertical cross section to demonstrate the formation of the gas jet. In Fig. 10(a), the component of wall stress caused by the spray jet is depicted. At an impact distance of 11 mm, the wall stress is concentrated within a small region where the impact occurs, indicating a finite level of stress. However, at a farther downstream location (e.g., 21 mm), the impacted region widens due to the radial expansion of the spray plume. Simultaneously, the stress level diminishes as the momentum of the spray jet decreases further downstream.

In contrast to the spray-jet-induced stress, the gas-jet-induced wall stress depicted in Fig. 10(b) is a consistent effect resulting from the static pressure of the gas phase. As a result, a finite level of wall stress is observed across the entire body of the ignition assistance device. The stress level varies from positive to negative values, while the spray-jet-induced stress only varies from zero to positive values. The positive stress observed at the impact zone signifies that the gas jet collides with that particular location, creating a stagnation point. At this stagnation point, the gas jet's momentum, or dynamic pressure, transforms into static pressure, contributing to positive values of normal stress. Furthermore, owing to the cylindrical shape of the ignition assistance device, the gas jet circulates around the body, as indicated by the arrow in Fig. 10(b). This high-velocity flow tangent to the surface results in a pressure decrease below the ambient pressure, leading to a continuous presence of negative relative pressure outside the stagnation point.

In Fig. 10, it is worth noting that both the gas-jet-induced and spray-jet-induced wall stresses reach an order of magnitude of 4 in their contour-scaled maxima when the impact distance is 11 mm.
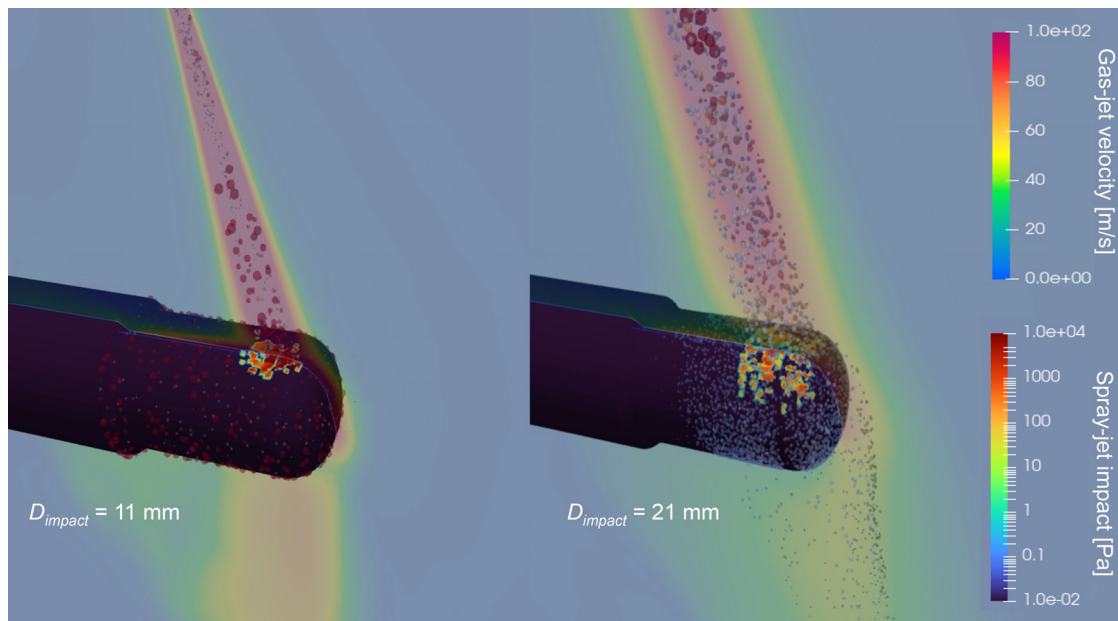
(a) Spray-jet induced stress
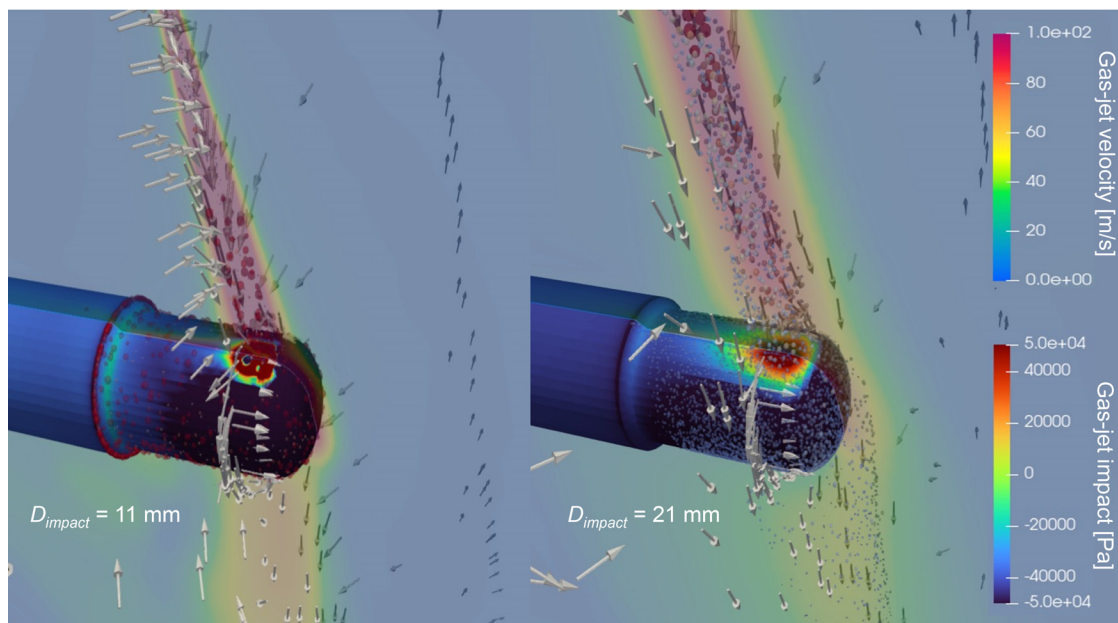
(b) Gas-jet induced stress

FIG. 10. (a) Spray-jet-induced and (b) gas-jet-induced wall stress formation under non-reacting conditions. Two impact distances are employed at 11 and 21 mm.

This suggests that the spray-induced wall stress can be comparable to the gas-jet-induced wall stress when the spray impact is intense. However, at a farther downstream condition, such as an impact distance of 21 mm, the spray-jet-induced wall stress becomes weaker. To quantify this trend, Fig. 11 illustrates the time-averaged wall stress on the ignition assistance device in the longitudinal (x) and circumferential

(θ) directions. The directional axes are defined with respect to the cylindrical component of the ignition assistance device's heating element, as depicted in the figure. The time-averaged wall stress component is divided into the gas-jet impact (red) and the spray-jet impact (green), calculated over the injection duration of 2.2 ms. Each measuring point represents a 0.1 mm spacing, and the wall stress values are collected
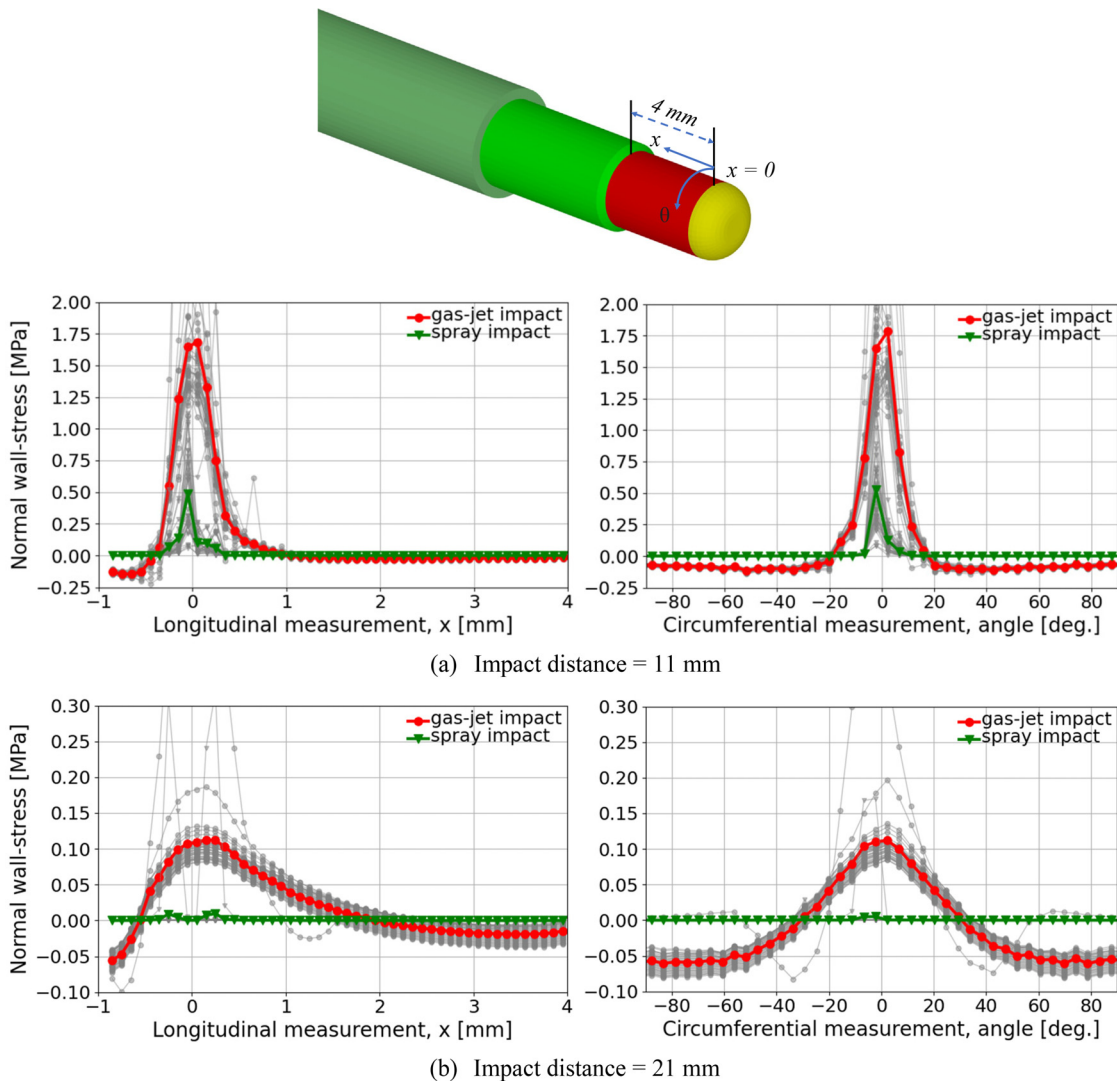
FIG. 11. Wall-stress distribution in longitudinal (x) and circumferential (θ) directions using two impact distance setups: (a) 11 and (2) 21 mm. Colored lines indicate time-averaged stress. Light grays indicate instantaneous stress profiles.

from neighboring cells. The light gray lines indicate the instantaneous profiles of wall stress variation at intervals of 0.1 ms.

From the results, it is observed that the peak value of the spray-induced wall stress reaches approximately one-third of the maximum gas-jet-induced wall stress for the impact distance of 11 mm. This indicates a significant contribution from the spray-jet impact. Conversely, for the farther downstream impact distance of 21 mm, the spray-jet impact becomes marginal on the wall stress, as shown in Fig. 11(b). In the 11 mm case, the spray-jet contributes to a non-zero level of wall stress only within a longitudinally 1 mm range, which is smaller compared to the impact distance of the 21 mm case. This is because the spray plume has not expanded radially enough to cover a broader range in the shallow impact distance scenario. On the other hand, the gas-jet impact is more spatially extended since the spray-jet is accompanied by the turbulent

gas-jet, creating a broader stagnation point. It is important to note that the gas-jet generates negative wall stress beyond the stagnation point. This occurs because the gas-jet continues to flow tangentially along the wall after impingement, as illustrated in Fig. 10(b). The accelerating flow from the stagnation point leads to a decrease in static pressure adjacent to the wall. This pressure decrease becomes more pronounced where the flow encounters a rounded wall, such as the end-tip of the ignition assistance device and the sidewall.

These findings imply that the spray-induced wall stress should be considered in the comprehensive structural analysis. However, this important engineering aspect has not been previously included in the studies on structural analysis.[35,36] Therefore, future studies incorporating the analysis of spray-induced wall stress can provide a more essential understanding for subsequent failure analysis of the system.

C. Wall-stress test on ignition assistance device: Reacting case

In this test, the wall-stress analysis is conducted under a reacting spray condition. For this purpose, the ignition assistance device heating element is activated by applying a voltage input of 7 V to the electric circuit. As a result, a thermal boundary layer forms around the ignition assistance device, which modifies the thermal properties of the mixture to aid in ignition assistance. The maximum temperature on the wall surface reaches 1400 K, which has been validated against experimental data in a previous study.[57] Meanwhile, the boundary condition of the injector remains the same as in the non-reacting test case. Therefore, the following discussion provides a comparative analysis of the mechanical stress formation, taking into account the impact on the hot surface of the device and subsequent combustion.

Figure 12 illustrates the pressure-rise history in the combustion chamber for two different impact distances: 11 and 21 mm. It is evident that the ignition timing varies significantly with the different impact distances. The impact distance of 21 mm (represented by the red solid line) results in faster ignition compared to the upstream impact distance of 11 mm (represented by the red dashed line). As a consequence, the pressure curve associated with the 21 mm impact distance exhibits a slow ramp-up profile, indicative of a moderately mixing-controlled combustion regime. In contrast, the 11 mm impact distance leads to delayed ignition and an explosive combustion regime driven by auto-ignition. This distinction can be attributed to the variation in the location of the thermal boundary layer, which influences the fuel–air mixing history and thermochemical properties.

Under the same injector boundary condition, the thermal boundary layer established upstream (e.g., 11 mm) encounters a richer air–fuel mixture and a denser liquid spray jet, creating a low-reactivity environment. Consequently, the fuel–air mixture travels further downstream of the ignition assistance device and spontaneously forms an ignition pocket when it encounters favorable conditions for auto-ignition. The flame kernel then grows following the most reactive mixture conditions, particularly the stoichiometric mixture along the periphery of the spray, as depicted in Fig. 13(a).
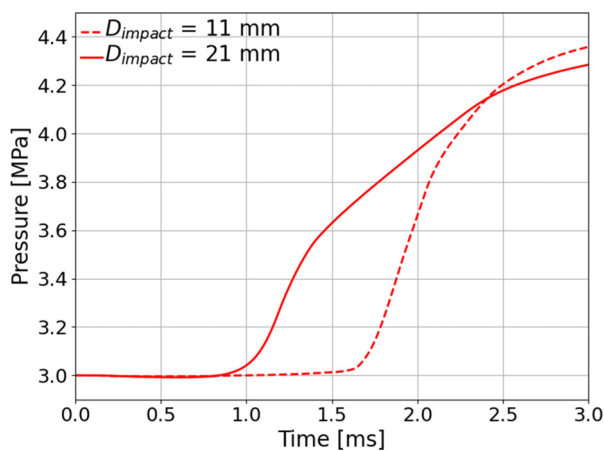

FIG. 12. Pressure trace in the combustion chamber (Ignition assistance device input voltage = 7 V).

On the other hand, the thermal boundary layer established downstream (e.g., 21 mm) heats a well-mixed fuel vapor and is less influenced by the liquid spray jet. This condition allows for a longer residence time for mixing, facilitating complete atomization and evaporation. As a result, the thermochemical properties of the mixture are more conducive to combustion within the thermal boundary layer. Consequently, an ignition pocket forms on the surface of the ignition assistance device, and the ignition kernel subsequently grows downward, following the most reactive stoichiometric mixture elements, as illustrated in Fig. 13(b). Since the evolution of the spray jet accompanies the growth of the ignition kernel, this combustion regime can be characterized as fully mixing-controlled.

The analysis conducted on the non-reacting condition, as shown in Fig. 10, also applies to the reacting condition. Therefore, Fig. 14 illustrates the time-averaged wall stress on the heating element of the ignition assistance device in the longitudinal (x) and circumferential (θ) directions. In contrast to the non-reacting case, the wall stresses induced by the gas jet (represented in red) and the spray jet (represented in green) are averaged over the injection period prior to ignition, thereby excluding the influence of pressure rise due to combustion. The red dashed lines represent the separate effects of combustion-induced wall stress at two different timings, specifically 2.0 and 3.0 ms.

The time-averaged wall stress component is separated into the impacts of the gas jet (red) and the spray jet (green), and it is averaged over the injection duration of 2.2 ms. Comparing Figs. 11 and 14, the wall stress profiles in both directions remain similar, with the reacting case showing a slight reduction in peak stress values. This reduction can be attributed to the presence of the hot thermal boundary layer formed around the ignition assistance device body. The hot surface and ambient air promote fuel evaporation, resulting in less liquid spray jet impinging on the wall. Additionally, the hot ambient air decreases the density of the surrounding gas, leading to a slight reduction in the impact of the gas jet on wall stress. Nevertheless, the current results support the previous claim that the wall stress induced by the spray jet may be significant when the impact distance is short. After ignition, the gas pressure in the combustion chamber rapidly increases due to the exothermic reaction. This elevated gas pressure applies a greater load to the entire ignition assistance device body, resulting in a quick growth of wall stress. This trend is represented by the red dashed lines at two different timings, 2 and 3 ms.

Based on the current analysis, it is evident that the spray jet induces substantial wall stress formation when it impinges on the wall at a shallow distance. Since the spray jet-induced ambient air entrainment also contributes to the gas jet, the combined effects of the gas jet and spray jet-induced wall stress should be considered a major source of structural fatigue in the system. Moreover, this intense wall stress is concentrated in a small area at the stagnation point of the jet impingement, which could lead to system operation failures (such as short circuits) or mechanical breakdowns. Therefore, the proposed SIWS model can provide a reasonable estimation of the mechanical load that should be taken into account during system design.

V. CONCLUSIONS

This study proposed a new wall-stress model, the SIWS model, which can account for the spray-jet-induced wall stress formation on a rigid body wall. The proposed model was successfully embedded into a Lagrangian spray modeling framework. The following paragraphs
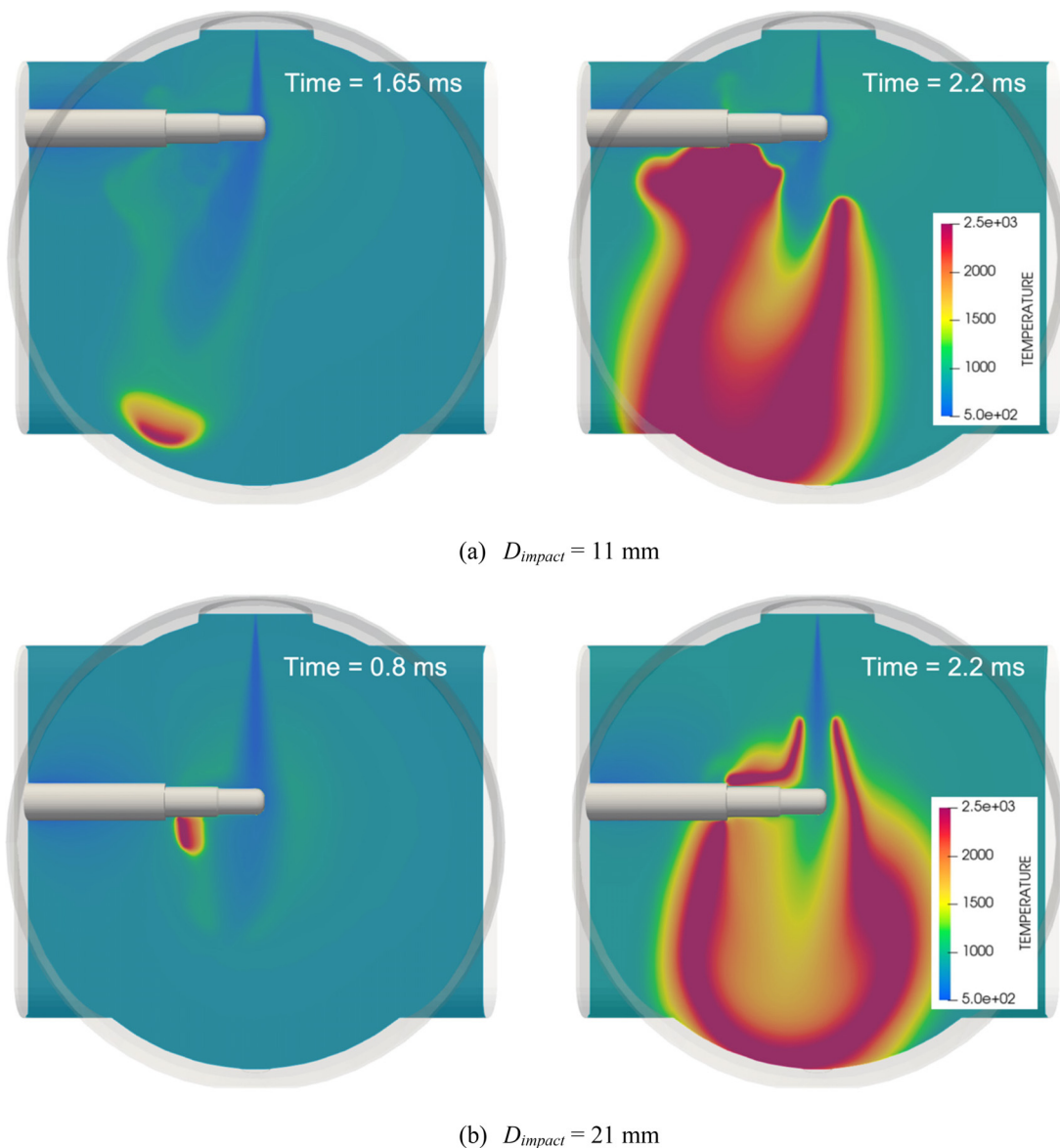
(a) D_{impact} = 11 mm

(b) D_{impact} = 21 mm

FIG. 13. Ignition pocket formation (left) and fully developed spray flame (right) using two impact distance setups: (a) 11 and (2) 21 mm, and ignition assistance device input voltage of 7 V.

summarize key takeaways gained from the numerical simulations and subsequent data analysis performed in this study.

The SIWS (Spray-Induced Wall Stress) model represents a significant advancement in understanding the formation of wall stress caused by spray impact. Previous literature primarily focused on wall stress resulting from gas pressure, but the SIWS model incorporates the momentum transfer of spray particles as an additional influential factor. This impinging spray impulse can generate substantial mechanical stress on the wall. The model assumes a seamless transfer of momentum from the spray particles to the wall-stress component, allowing the transmitted momentum to be redefined in terms of stress

units. The successful integration of the SIWS model into the widely used CONVERGE commercial CFD software enables the estimation and storage of wall-stress values within the software's boundary cells.

This study successfully validated the proposed model. The initial step involved verifying the basic Lagrangian spray model setup against available data on spray penetrating length. Subsequently, the SIWS model was integrated into the basic setup. The tested SIWS model demonstrated accurate prediction of the experimentally measured rate of momentum (impulse force) across various injector configurations. However, it is important to note that the simplified physics employed in the mathematical description may lead to errors when dealing with
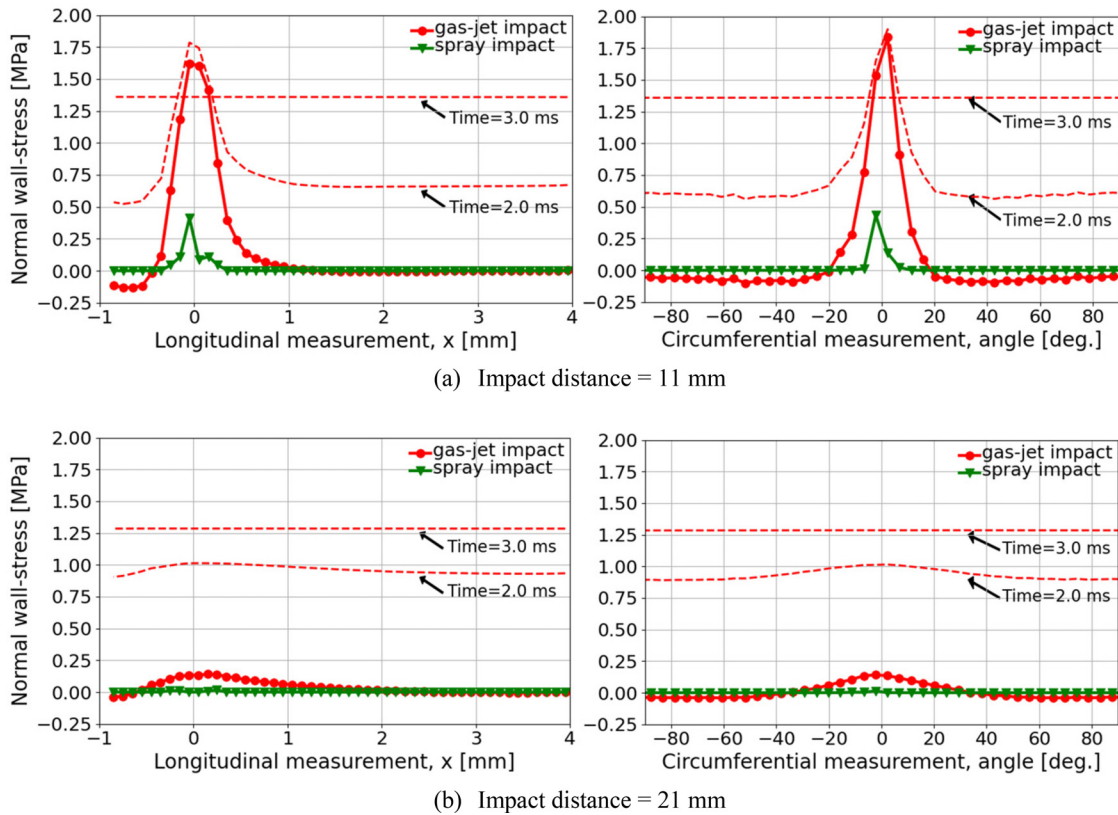
(a) Impact distance = 11 mm

(b) Impact distance = 21 mm

FIG. 14. Wall-stress distribution in longitudinal (x) and circumferential (θ) directions using two impact distance setups: (a) 11 and (2) 21 mm. Red dashed line indicates the instantaneous wall-stress level applied with the gas-jet impact only.

larger injector hole sizes, which result in the presence of large liquid particles. In such scenarios, the proposed model may not adequately account for the complex physics associated with mechanical energy and thermal energy dissipation.

The study's discussion distinguishes between the sources of wall stress, specifically the gas-jet impact and spray-jet impact. The gas-jet is formed as a result of the gas entrainment caused by the high-flux spray jet. Previous literature focused solely on analyzing the impact of the gas-jet on wall stress, as they lacked the capability to consider the spray-jet impact. However, the inclusion of the SIWS model in the current simulations enabled the analysis of spray-jet impact. The results demonstrate that both the spray-jet and gas-jet impacts significantly contribute to the resulting wall stress profile, particularly in scenarios where the impact distance is relatively shallow.

The SIWS model was employed to analyze the wall stress characteristics in the ignition enhancement system of aircraft propulsion systems. Within the combustion chamber, an ignition assistance device was installed, and the spray jet impinged on the heating element of the device. Non-reacting and reacting simulations were conducted to examine the behavior. The simulation results indicate that the wall stress induced by the spray jet can be as significant as the impact from the gas-jet when the impact distance is short. This high level of wall stress is concentrated in a small area of the spray-impinging region. From a structural

analysis perspective, the SIWS model offers an effective solution. The simulated outcomes emphasize that the high-pressure spray jet has the potential to generate intense and localized wall stress accumulation. This, in turn, may lead to fatigue in the solid materials and ultimately result in system failure.

and perform publicly and display publicly, by or on behalf of the Government. The Department of Energy will provide public access to these results of federally sponsored research in accordance with the DOE Public Access Plan. http://energy.gov/downloads/doe-public-access-plan. The views and conclusions presented in this document are solely those of the authors and do not necessarily reflect the official policies of the Army Research Laboratory or the U.S. Government. The U.S. Government has the right to reproduce and distribute reprints of this work for governmental purposes, regardless of any copyright notation included.

AUTHOR DECLARATIONS
Conflict of Interest

The authors have no conflicts to disclose.

Author Contributions

Soup Kim: Conceptualization (equal); Data curation (equal); Formal analysis (equal); Investigation (equal); Methodology (equal); Software (equal); Validation (equal); Visualization (equal); Writing – original draft (equal); Writing – review & editing (equal). **Roberto Torelli:** Conceptualization (equal); Investigation (supporting); Supervision (equal). **Surya Kaundinya Oruganti:** Validation (supporting). **Je Ir Ryu:** Funding acquisition (equal); Supervision (equal). **Tonghun Lee:** Resources (supporting). **Kenneth S. Kim:** Project administration (equal); Supervision (supporting). **Chol-Bum M. Kweon:** Project administration (equal); Supervision (equal).

DATA AVAILABILITY

The data that support the findings of this study are available from the corresponding author upon reasonable request.

REFERENCES

[1]S. Wei, L. Sun, L. Wu, Z. Yu, and Z. Zhang, "Study of combustion characteristics of diesel, kerosene (RP-3) and kerosene-ethanol blends in a compression ignition engine," Fuel **317**(1), 123468 (2022).

[2]Z. Zhao and H. Cui, "Numerical investigation on combustion processes of an aircraft piston engine fueled with aviation kerosene and gasoline," Energy **239**, 122264 (2022).

[3]L. Chen, M. Raza, and J. Xizo, "Combustion analysis of an aviation compression ignition engine burning pentanol–kerosene blends under different injection timings," Energy Fuels **31**(9), 9429–9437 (2017).

[4]Z. Kan, Z. Hu, D. Lou, P. Tan, Z. Cao, and Z. Yang, "Effects of altitude on combustion and ignition characteristics of speed-up period during cold start in a diesel engine," Energy **150**(1), 164–175 (2018).

[5]B.-X. Lin, Y. Wu, M.-X. Xu, and Y.-M. Shen, "Experimental investigation on high-altitude ignition and ignition enhancement by multi-channel plasma igniter," Plasma Chem. Plasma Process. **41**, 1435–1454 (2021).

[6]Z. Xu, F. Ji, S. Ding, Y. Zhao, X. Zhang, Y. Zhou, Q. Zhang, and F. Du, "High-altitude performance and improvement methods of poppet valves 2-stroke aircraft diesel engine," Appl. Energy **276**, 115471 (2020).

[7]U.S. Department of Defense, "DoD management policy for energy commodities and related services section 4.2: Fuel standardization," No. 4140.25 (U.S. Department of Defense, Washington D.C., 2004.

[8]U.S. Department of Defense, "Detail specification turbine fuel, aviation, kerosene Type JP-8 (NATO F-34), NATO F-35, and JP-8 + 100 (NATO F-37)," No. MIL-DTL-83133F, 2015.

[9]R. D. Meininger, C.-B. M. Kweon, M. T. Szedlmayer, K. Q. Dang, N. B. Jackson, C. A. Lindsey, J. A. Gibson, and R. H. Armstrong, "Knock criteria for aviation diesel engines," Int. J. Engine Res. **18**(7), 752–762 (2017).

[10]R. Rajasegar, Y. Niki, Z. Li, J. M. Garcia-Oliver, and M. P. B. Musculus, "Influence of pilot-fuel mixing on the spatio-temporal progression of two-stage autoignition of diesel-sprays in low-reactivity ambient fuel-air mixture," Proc. Combust. Inst. **38**, 5741–5750 (2021).

[11]S. Kim, R. Scarcelli, Y. Wu, J. Rohwer, A. Shah, T. Rockstroh, and T. Lu, "Simulations of multi-mode combustion regimes realizable in a gasoline direct injection engine," J. Energy Resour. Technol. **143**, 112307 (2021).

[12]Q. Li, P. Shayler, M. McGhee, and A. La Rocca, "The initiation and development of combustion under cold idling conditions using a glow plug in diesel engines," Int. J. Engine Res. **18**(3), 240–255 (2017).

[13]S. X. Cheng and J. S. Wallace, "Transient behavior of glow plugs in direct-injection natural gas engines," J. Eng. Gas Turbines Power **134**(9), 092802 (2012).

[14]J. Li, C. Gong, Y. Su, H. Dou, and X. Liu, "Effect of preheating on firing behavior of a spark-ignition methanol-fueled engine during cold start," Energy Fuels **23**(11), 5394–5400 (2009).

[15]E. R. Amezcua, K. Kim, D. Rothamer, and C.-B. M. Kweon, "Ignition sensitivity analysis for energy-assisted compression-ignition operation on jet fuels with varying cetane number," SAE Int. J. Adv. Curr. Practices Mobility **4**(5), 1651–1666 (2022).

[16]N. Miganakallu, J. Stafford, E. Amezcua, K. S. Kim, C.-B. M. Kweon, and D. Rothamer, "Impact of ignition assistant on combustion of Cetane 30 and 35 jet-fuel blends in a compression-ignition engine at moderate load and speed," J. Eng. Gas Turbines Power **145**(7), 071013 (2023).

[17]H. D. Sapra, R. P. Hessel, E. R. Amezcua, J. Stafford, N. Miganakallu, D. Rothamer, K. Kim, C.-B. M. Kweon, and S. Kokjohn, "Numerical modeling and analysis of energy-assisted compression ignition of varying cetane number jet fuels for high-altitude operation," J. Eng. Gas Turbines Power **145**, 091004 (2023).

[18]J. I. Ryu, A. H. Motily, R. Scarcelli, S. Som, K. S. Kim, C.-B. M. Kweon, and T. Lee, "Ignition enhancement of F-24 jet fuel by a hot surface for aircraft propulsion systems," AIAA Paper No. 2020-2142, 2020.

[19]J. I. Ryu, A. H. Motily, T. Lee, R. Scarcelli, S. Som, K. S. Kim, and C.-B. Kweon, "Effect of hot probe temperature on ignition of alcohol-to-je (ATJ) fuel spray under aircraft propulsion system conditions," AIAA Paper No. 2021-0985, 2021.

[20]A. Motily, J. I. Ryu, K. Kim, K. S. Kim, C.-B. M. Kweon, and T. Lee, "High-pressure fuel spray ignition behavior with hot surface interaction," Proc. Combust. Inst. **38**(4), 5665–5672 (2021).

[21]J. I. Ryu, A. H. Motily, T. Lee, R. Scarcelli, S. Som, K. S. Kim, and C.-B. M. Kweon, "Ignition of jet fuel assisted by a hot surface at aircraft compression ignition engine conditions," AIAA Paper No. 2020-3889, 2020.

[22]A. H. Motily, J. I. Ryu, Y. Kim, K. S. Kim, T. Lee, and C.-B. M. Kweon, "Effects of cetane number on high-pressure fuel spray characteristics with a hot surface ignition source," AIAA Paper No. 2020-2280, 2020.

[23]C. Oprea, F. Wong, H. K. Sharif, C. Blair, A. Welch, and T. Troczynsk, "Degradation of silicon nitride glow plugs in various environments—Part 3: NGDI engine," Int. J. Appl. Ceram. Technol. **9**(2), 272–279 (2012).

[24]A. H. Motily, "Evaluation of hot surface ignition device performance with high-pressure kerosene fuel sprays," M.S. dissertation (University of Illinois at Urbana-Champaign, 2020).

[25]B. Karpe, D. Klobčar, J. Kovač, M. Bizjak, B. Kosec, and S. Vesković-Bukudur, "Failure analysis of diesel engine glow plugs," Eng. Failure Anal. **109**, 104394 (2020).

[26]J. A. Dixon, J. A. Verdicchio, D. Benito, A. Karl, and K. M. Tham, "Recent developments in gas turbine component temperature prediction models, using computational fluid dynamics and optimization tools, in conjunction with more conventional finite element analysis techniques," Proc. Inst. Mech. Eng., Part A **218**(4), 241–255 (2004).

[27]M. Bielecki, M. Karcz, W. Radulski, and J. Badur, "Thermomechanical coupling between the flow of steam and deformation of the valve during start-up of the 200 mw turbine," TASK Q. **5**(2), 125–140 (2001).

[28]M. Diefenthal, P. Łuczyński, C. Rakut, M. Wirsum, and T. Heuer, "Thermomechanical analysis of transient temperatures in a radial turbine wheel," J. Turbomach. **139**(9), 091001 (2017).

[29]D. Amirante, N. J. Hills, and C. J. Barnes, "Thermo-mechanical finite element analysis/computational fluid dynamics coupling of an interstage seal cavity using torsional spring analogy," J. Turbomach. **134**(5), 051015 (2012).

19 October 2023 11:31:27

[30]X. Luo, X. Zheng, P. Zou, Y. Lin, T. Wei, X. Yuan, and S. Liao, "A finite element analysis-computational fluid dynamics coupled analysis on thermal-mechanical fatigue of cylinder head of a turbo-charged diesel engine," Proc. Inst. Mech. Eng., Part D **234**(6), 1634–1643 (2020).

[31]M. Fadaei, H. Vafadar, and A. Noorpoor, "New thermo-mechanical analysis of cylinder heads using a multi-field approach," Sci. Iran. **18**(1), 66–74 (2011).

[32]A. Belhocine and M. Bouchetara, "Thermal–mechanical coupled analysis of a brake disk rotor," Heat Mass Transfer **49**, 1167–1179 (2013).

[33]J. Tang, D. Bryant, and H. Qi, "Coupled CFD and FE thermal mechanical simulation of disc brake," in EuroBrake 2014 Conference, Lille, France, 2014.

[34]L. Wang, C. Zheng, S. Wei, B. Wang, and Z. Wei, "Thermo-mechanical investigation of composite high-pressure hydrogen storage cylinder during fast filling," Int. J. Hydrogen Energy **40**(21), 6853–6859 (2015).

[35]S. G. Kang, J. I. Ryu, A. H. Motily, P. Numkiatsakul, T. Lee, W. M. Kriven, K. S. Kim, and C.-B. M. Kweon, "Thermomechanical characterization of hot surface ignition device using phenomenological heat flux model," J. Propul. Power **38**(4), 656–670 (2022).

[36]S. G. Kang, J. I. Ryu, A. H. Motily, P. Numkiatsakul, T. Lee, W. M. Kriven, K. S. Kim, and C.-B. M. Kweon, "Transient thermomechanical stress analysis of hot surface ignition device using sequentially coupled computational fluid dynamics-finite element analysis approach," J. Eng. Gas Turbines Power **145**, 121001 (2023).

[37]T. Ma, L. Feng, H. Wang, H. Liu, and M. Yao, "A numerical study of spray/wall impingement based on droplet impact phenomenon," Int. J. Heat Mass Transfer **112**, 401–412 (2017).

[38]J. Kim, J. Chung, J. Lee, S. Moon, and K. Min, "Modeling of spray wall impingement and fuel film formation under the gasoline direct injection condition," Atomization Sprays **32**(3), 25–52 (2022).

[39]S.-Y. Chen, D.-Q. Zhu, H.-J. Xing, Q. Zhao, Z.-F. Zhou, and B. Chen, "Droplet formation and impingement dynamics of low-boiling refrigerant on solid surfaces with different roughness under atmospheric pressure," Appl. Sci. **12**, 8549 (2022).

[40]M. Angelino, P. Fernández-Yáñez, H. Xia, and G. J. Page, "Large-eddy simulation with modeled wall stress for complex aerodynamics and stall prediction," AIAA J. **59**(4), 1225 (2021).

[41]R. Payri, S. Ruiz, F. J. Salvador, and J. Gimeno, "On the dependence of spray momentum flux in spray penetration: Momentum flux packets penetration model," J. Mech. Sci. Technol. **21**, 1100–1111 (2007).

[42]R. Payri, G. Bracho, P. Martí-Aldaraví, and A. Moreno, "Using momentum flux measurements to determine the injection rate of a commercial urea water solution injector," Flow Meas. Instrum. **80**, 101999 (2021).

[43]F. Luo, H. Cui, and D. Dong, "Transient measuring method for injection rate of each nozzle hole based on spray momentum flux," Fuel **125**(1), 20–29 (2014).

[44]B. W. Knox, M. J. Franze, and C. L. Genzale, "Diesel spray rate-of-momentum measurement uncertainties and diagnostic considerations," J. Eng. Gas Turbine Power **138**(3), 031507 (2016).

[45]L. Postrioti, M. Battistoni, C. Ungaro, and A. Mariani, "Analysis of diesel spray momentum flux spatial distribution," SAE Int. J. Engines **4**(1), 720–736 (2011).

[46]L. Postrioti, F. Mariani, and M. Battistoni, "Experimental and numerical momentum flux evaluation of high pressure diesel spray," Fuel **98**, 149–163 (2012).

[47]K. J. Richards, P. K. Senecal, and E. Pomraning, *CONVERGE, ver. 3.0.27* (Convergent Science, Madison, WI, 2023).

[48]P. J. O'Rourke and A. A. Amsden, "A spray/wall interaction submodel for the KIVA-3 wall film model," SAE Int. J. Engines **109**(3), 281–298 (2000).

[49]J. C. Beale and R. D. Reitz, "Modeling Spray Atomization with the Kelvin-Helmholtz/Rayleigh-Taylor Hybrid Model," Atomization and Sprays **9**(6), 623–650 (1999).

[50]N. Frossling, "The evaporation of falling drops," J. Geophys. Res. **52**, 170–216 (1938).

[51]D. J. Valco, K. Min, A. Oldani, T. Edwards, and T. Lee, "Low temperature autoignition of conventional jet fuels and surrogate jet fuels with targeted properties in a rapid compression machine," Proc. Combust. Inst. **36**(3), 3687–3694 (2017).

[52]J. I. Ryu, K. Kim, R. Scarcelli, S. Som, K. S. Kim, J. E. Temme, C.-B. M. Kweon, and T. Lee, "Data-driven chemical kinetic reaction mechanism for F-24 jet fuel ignition," Fuel **290**, 119508 (2021).

[53]H. Wang, R. Xu, K. Wang, C. T. Bowman, R. K. Hanson, D. F. Davidson, K. Brezinsky, and F. N. Egolfopoulos, "A physics based approach to modeling real-fuel combustion chemistry—I: Evidence from experiments and thermodynamics, chemical kinetics and statistical considerations," Combust. Flame **193**, 502–519 (2018).

[54]H. Blumberg, "Hausdorff's Grundzüge der Mengenlehre," Bull. Am. Math. Soc. **27**(3), 116–129 (1920).

[55]C. Bai and A. Gosman, "Mathematical modeling of wall films formed by impinging sprays," J. Engines **105**(3), 782–796 (1996).

[56]D. Kuhnke, "Spray/wall-interaction modelling by dimensionless data analysis," Ph.D. dissertation (Technical University of Darmstadt, 2004).

[57]S. Kim, J. I. Ryu, A. Motily, P. Numkiatsakul, R. Alonso, T. Lee, W. Kriven, K. S. Kim, and C.-B. M. Kweon, "Effect of heating device voltage on fuel spray ignition and flame characteristics under aviation propulsion system conditions," AIAA Paper No. 2023-1652, 2023.

[58]A. MoMly, E. J. Wood, J. I. Ryu, K. S. Kim, and C.-B. Kweon, OpMmizing hot-surfaceassisted igniMon performance of high-pressure F-24 fuel sprays," AIAA SciTech Forum, Virtual Event, AIAA 2021–0414 (2021).

[59]S. Kim, J. I. Ryu, A. H. MoMly, T. Lee, K. S. Kim, and C.-B. M. Kweon, "Parametric analysis on igniMon assistance by a shielded hot surface under aircraq compression igniMon engine condiMons," 14th Asia-Pacific Conference on CombusMon, Kaohsiung, Taiwan, May 14–18 (2023).

[60]S. G. Kang, J. I. Ryu, A. MoMly, P. Numkiatsakul, T. Lee, W. Kriven, K. S. Kim, and C.-B. Kweon, "Thermo-mechanical response of a hot surface igniMon device under aircraq compression igniMon engine condiMons," AIAA Propulsion and Energy Forum, Virtual Event, AIAA 2021–3615 (2021).

19 October 2023 11:31:27